# Slurry Abrasion and Dry Sliding Behavior of High-Velocity Oxy-Fuel (HVOF) Sprayed WC-12Co and WC-10Co-4Cr Coatings on EN8 Tillage Material

Honey Khan[1] · Jaspal Singh Gill[1] · Anuj Bansal[1] · Vikrant Singh[1]

**Abstract** This research focuses on enhancing the wear resistance of EN8 steel, commonly used in agricultural implements by applying WC-12Co and WC-10Co-4Cr coatings using the high-velocity oxy-fuel (HVOF) spraying technique. The microstructural characterization, EDS mapping, microhardness, fracture toughness, slurry abrasion, and dry sliding of all coated and uncoated samples were evaluated. Results demonstrate that coated specimens outperform the uncoated EN8 steel in terms of wear resistance. Slurry abrasion tests reveal that the coatings hardness and fracture toughness contribute to their excellent performance. In dry sliding tests, the coated specimens exhibit lower friction coefficients and less mass loss, further emphasizing their better wear resistance. Further, wear mechanisms were found to be different between the materials, with EN8 steel exhibiting ductile wear, primarily due to plastic deformation and chipping, while the coated specimens display brittle wear characteristics, with the detachment of hard coating material and abrasive interactions contributing to wear.

**Keywords** EN8 · HVOF · slurry and dry sliding wear · WC-12Co · WC-10Co-4Cr

✉ Jaspal Singh Gill
jsgillsliet@gmail.com

1  Sant Longowal Institute of Engineering and Technology, Longowal, Punjab, India

## Introduction

The agricultural sector, also known as the farm industry, plays a pivotal role in sustaining human life by providing essential food and raw materials (Ref 1, 2). It is not merely an industry but a cornerstone of civilization, with a profound impact on economies and societies worldwide (Ref 3, 4). The cultivation of crops and the management of livestock are the core activities of the farm industry, and to execute these tasks efficiently, modern agriculture relies heavily on mechanized equipment, including tillage machinery (Ref 5, 6). These machines are the backbone of farming, helping farmers to prepare the soil for planting, manage weeds, and enhance overall crop yields. The significance of the farm industry in feeding growing populations and supporting rural livelihoods cannot be overstated (Ref 7, 8). However, the agricultural sector faces persistent challenges, particularly with regard to the wear and abrasion of tillage equipment. These issues have far-reaching implications for both the productivity and livelihood of farmers. Tillage equipment, such as plows, cultivators, and harrows, are exposed to a harsh operational environment (Ref 9, 10). As they interact with the soil, stones, and abrasive particles, they experience severe wear and tear. This wear not only reduces the equipment's effectiveness but also imposes substantial economic burdens on farmers due to repair and replacement costs. The persistence of these problems not only hampers the efficiency of farming operations but also affects the income and well-being of farmers (Ref 11, 12).

Slurry wear involves the gradual removal of material from a surface due to the impact of abrasive particles or fluids, often resulting in the degradation of the surface over time. On the other hand, abrasion wear specifically refers to the mechanical wearing down of a surface through repeated

frictional contact with another surface or abrasive particles, leading to material loss and surface damage (Ref 13). The extent of wear and abrasion in tillage equipment can vary widely, depending on several critical parameters. The type of soil encountered during tillage operations, such as clay, sandy, or rocky soils, can have a significant impact on equipment wear (Ref 14). The abrasive nature of soil particles and the presence of rocks can accelerate equipment degradation. The load applied to tillage equipment during operations, as well as the equipment's design and material, influence wear resistance (Ref 15, 16). High-speed and frequent use, environmental conditions like moisture content and temperature, and the quality of maintenance also play vital roles in determining wear rates. To tackle the problem of wear and abrasion in tillage equipment, advanced thermal spray coatings offer a promising solution (Ref 17, 18). Among these coatings, tungsten carbide (WC) stands out for its exceptional hardness, toughness, and wear resistance. When combined with cobalt (Co) or cobalt-chromium (Co-Cr) and applied using the high-velocity oxy-fuel (HVOF) thermal spraying technique, WC-based coatings provide superior protection against wear and abrasion (Ref 19, 20). The significant contribution of thermal spray coatings in agriculture is undeniable. These coatings act as a first line of defense, preserving equipment integrity, reducing maintenance costs, and enhancing farming efficiency (Ref 21). The HVOF process is renowned for producing dense, high-quality coatings with excellent adhesion and minimal porosity. When WC-based coatings are HVOF-sprayed onto substrate steel, they have the potential to substantially mitigate erosive wear experienced by tillage equipment (Ref 22, 23). These coatings offer exceptional hardness, wear resistance, and resistance to corrosion and chemical attack. The integration of such coatings on equipment components can significantly reduce the detrimental effects of wear, leading to longer-lasting and more cost-effective solutions for farmers (Ref 24, 25).

The novelty of this research lies in its unique approach in addressing the challenges faced by the agricultural industry. Although different methods have been employed for improving the hardness of the surface and thus wear resistance. As highlighted in one of the research works, Suraj et al. (Ref 26) hard-faced the EN8 material using GTAW process with ER70S as the filler material, by adding Si and Mn to the surface and improving its wear resistance. Further, Rethnam et al. (Ref 27) has reported solid state surfacing by friction stir welding process where EN8 material was surfaced by SS316L. Also, effect of local remelting and recycled WC-Co composite reinforcement size on abrasive and erosive wear of manual arc welded hardfacings has also been reported by Katinas et al. (Ref 28). In the said research work, it has been reported

that up to 550 °C the coatings exhibited almost two times strongness for wear but at higher temperatures it gets softened. Moreover, 35CrMo steel substrate was also coated with WC-10Co powder by HVOF process by Ribu et al. (Ref 29), and it has been reported that the process was able to successfully improve the erosion resistance. Next, Goyal et al. (Ref 30) also reported an effective slurry erosion control by HVOF process for WC-based coatings. Hence, this research can be said to venturing into uncharted territory by focusing on the performance of WC-12Co and WC-10Co-4Cr coatings when applied to EN8 steel, which is a common substrate material for tillage equipment. This specific combination of coating materials and substrate has not been extensively explored in the context of protecting machinery used in tillage operations (Ref 25). Traditionally, studies in this domain have centered on single materials or coating processes. The current research takes a step further by comparing two distinct coating materials, WC-12Co and WC-10Co-4Cr, and analyzing their suitability for safeguarding EN8 steel against the abrasive conditions encountered in the field.

Therefore, in this research article, a comprehensive evaluation of two distinct WC-based coatings, WC-12Co and WC-10Co-4Cr, applied to EN8 steel, a representative substrate material for tillage equipment has been undertaken. The study investigates the performance of these coatings in slurry abrasion and dry sliding conditions, replicating the real-world challenges faced by farmers in agricultural machinery. By examining the abrasion resistance, dry sliding behavior, and wear mechanisms of these coatings, this research aims to provide valuable insights to the farm industry, helping enhance the durability and longevity of tillage equipment and ultimately improve the livelihoods of farmers.

## Materials and Methods

### Tillage Material and Coating Powders

Out of the various choices like AISI 1050, AISI 1070 carbon steels, and Boron steels, heat-treated EN8 steel is commonly used by agriculture industries in Punjab, India, to manufacture inexpensive agricultural implements like disk harrows (Ref 31). This may owe to its properties like lower cost, better machineability, acceptable surface hardness, and moderate wear resistance (Ref 31). Therefore, in this research work, EN8 has been selected as a substrate material and the same was purchased in form of rod of 10 mm diameter and plates of 50 mm width and 6 mm thickness from Bagri Alloy Steel Company, Chandigarh. The chemical composition of procured EN8 steel as obtained from the spectroscopy test is shown in

**Table 1** Chemical composition of as received EN8 steel as per spectroscopy test

| Element | C | Si | Mn | P | S | Fe |
|---|---|---|---|---|---|---|
| As received, wt.% | 0.42 | 0.31 | 0.84 | 0.049 | 0.047 | Remaining |

**Table 2** Properties of WC-12Co and WC-10Co-4Cr powders

| Designation | Type | Praxair product | Flow density | Size |
|---|---|---|---|---|
| WC-12Co | Sintered | WC 489-1 | 4.9 g/cm$^3$ in 16 s | 10 to 45 μm |
| WC-10Co-4Cr | Sintered | WC 436-1 | 4.5 g/cm$^3$ in 21 s | 10 to 45 μm |

Table 1. The obtained composition implies acceptability of the material as per ASTM standard composition (Ref 32). The rectangular sample having 57 × 25 × 6 mm size and cylindrical sample having 30 mm length and 8 mm diameter have been cut from the procured steel for slurry abrasion and dry sliding tests, respectively.

Commercially available WC-based powders like WC-12Co and WC-10Co-4Cr provide dense and hard coatings with excellent wear properties (Ref 33, 34). WC-12Co provides good wear properties with marginal oxidation and corrosion resistance (Ref 34). However, on the other hand, WC-10Co-4Cr provides good corrosion resistance and improved oxidation along with good wear resistance (Ref 35). Therefore, these materials have been chosen for modifying the surface of EN8 steel in this research work. The properties of the procured WC-12Co and WC-10Co-4Cr powders are shown in Table 2.

For analyzing the structure and composition of the procured powders, field-emission scanning electron microscope FESEM (JSM-7610Fplus, JEOL, Japan) along with the INCAx-act attachment for EDS analysis at Central Facility SLIET Longowal has been used. Figure 1 presents the SEM and EDS images of WC-12Co and WC-10Co-4Cr powders.

Figure 1(a) shows that WC-12Co powder has accumulated sintered and spherical morphology, which provides better flowability of 4.9 g/cm$^3$ in 16 s, as also presented in Table 3. Moreover, the SEM micrograph for WC-10Co-4Cr powder as depicted in Fig. 1(b) indicated an agglomeration and sintering process leading to an elongated spherical morphology. Owing to elongated spherical structure, the coating powder has comparatively lesser flowability of 4.5 g/cm$^3$ in 21 s. However, both the powders have enough flowability to pursue better coating depositions using the HVOF process. EDS analysis as presented in Fig. 1(c) and (d) validates the existence of W, C, and Co elements and W, C, Co, and Cr elements for WC-12Co and WC-10Co-4Cr powders, respectively, that associates to the said composition of coating powders. From SEM analysis, the particle size for both the powders was reported to be 15 to 45 μm. The carbon content in the

EDS analysis might have been observed owing to the carbon tape over which the powder sample has been deposited for the SEM and EDS analysis,

Further, the phase analysis of the coating powders has been carried out with the help of x-ray diffractometer (XRD) using BRUKER D-8 ADVANCE x-ray diffractometer and the graphs for WC-12Co and WC-10Co-4Cr powders, so obtained are presented in Fig. 2(a) and (b), respectively. As expected, for both the powders, major peaks correspond to WC as a primary element followed by existence of Co. Also, in case of WC-10Co-4Cr powder, the smaller peaks of Cr phase have also been noticed that justifies the existence of 4% Cr in the coating powder. Also, some low-intensity peaks of $Co_3W_3C$ and $Co_6W_6C$ after $2\Theta = 40°$ have been noticed for WC-10Co-4Cr powder.

## Preparation of Coatings

The prepared EN8 specimens (both rectangular and cylindrical pin) were coated with WC-12Co and WC-10Co-4Cr powders using HVOF spray gun system. To remove impurities and oxide scales from the surface of substrate and to provide better adhesion of coating splats with the base material, before the coating deposition, grit blasting was done using alumina oxide abrasives (size: − 1400 + 425 μm). Surface activation was done using Portable P7300 grit blasting machine. Afterward, the coatings have been carried out on HVOF spray system using ST-4000 gun (manufactured by CERDI, Belgium). Prior to the actual coating depositions, a number of trial runs were undertaken to identify a suitable combination of HVOF coating parameters. On the basis of visual inspection pertaining to uniform coating with no visual and surface defects like cracks and pores, the finalized combination of parameters for both the coatings has been selected and the same are presented in Table 3. These parameters are also in line with the existed studies (Ref 36). Coating was carried out with the help of a six-axis robot, which moves the spray gun back and forth in front of the fixed rectangular and cylindrical specimens and maintains the constant spray distance. The movement speed of

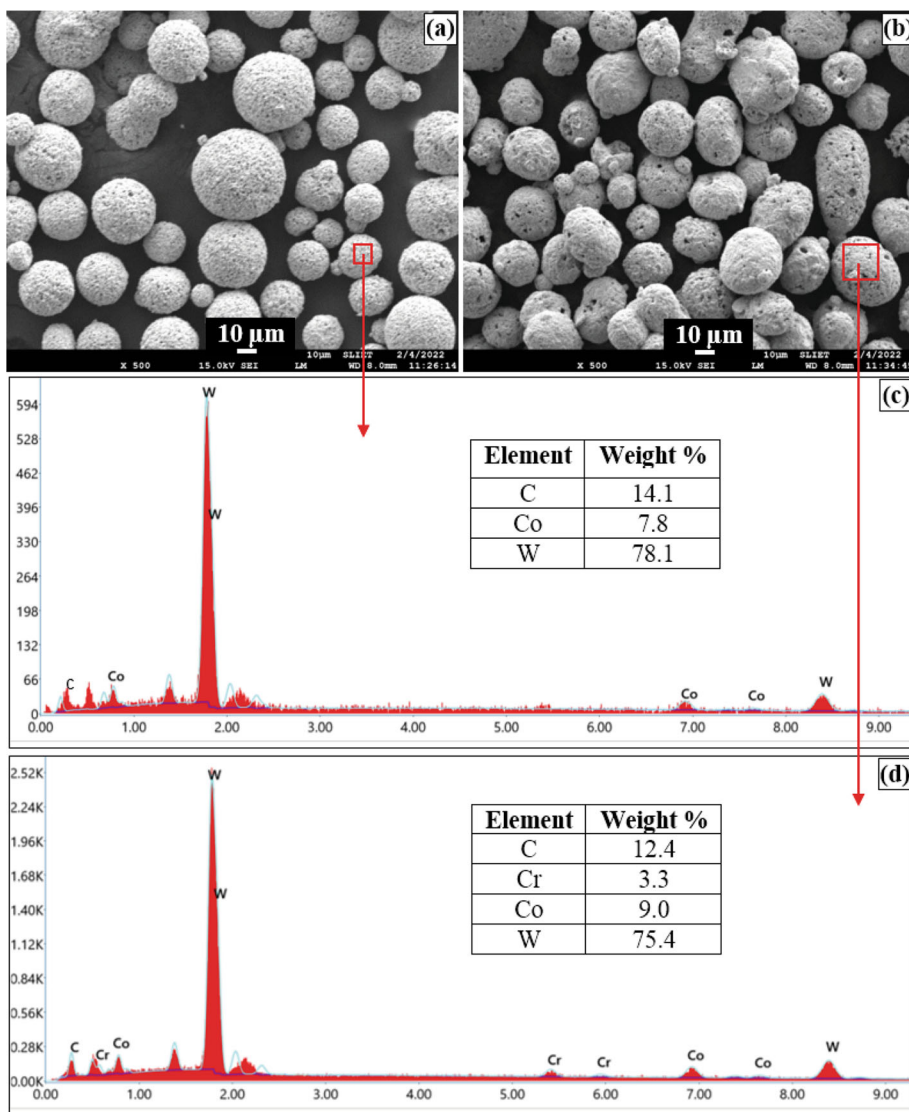**Fig. 1** SEM image and EDS analysis of (a), (c) WC-12Co and (b), (d) WC-10Co-4Cr powders, respectively



| Element | Weight % |
|---------|----------|
| C | 14.1 |
| Co | 7.8 |
| W | 78.1 |

| Element | Weight % |
|---------|----------|
| C | 12.4 |
| Cr | 3.3 |
| Co | 9.0 |
| W | 75.4 |

**Table 3** Parameters used for HVOF-sprayed WC-12Co and WC-10Co-4Cr coatings

| Spraying parameters | Fuel (Kerosene) flow rate | $O_2$ flow rate | $N_2$ flow rate | Spray distance | Powder feed rate | $H_2O$ flow rate |
|---------------------|---------------------------|-----------------|-----------------|----------------|------------------|------------------|
| WC-12Co | 20.4 l/h | 61.4 m$^3$/h | 0.65 m$^3$/h | 380 mm | 81 g/min | 37 l/h |
| WC-10Co-4Cr | 23.8 l/h | 56.1 m$^3$/h | 0.65 m$^3$/h | 380 mm | 70 g/min | 37 l/h |

the gun during depositing coatings was maintained as 10 mm/s. The coatings were carried out on the plane surface of rectangular and spherical tip of the cylindrical specimen as presented in Fig. 3. Moreover, the specimens were cooled during regular intervals using compressed air.

### Characterization of Prepared Coatings

To analyze the cross-sectional morphology of the prepared coatings, FESEM (JSM-7610Fplus, JEOL, Japan) was employed. Additionally, surface EDS analysis was conducted using an EDAX attachment with FESEM to examine the distribution of coating powder on the specimen surface. Coating thicknesses and percentage porosity of coatings were measured using cross-sectional SEM images with the assistance of ImageJ software. Fifteen measurements were taken for both thickness and porosity, and the average values were determined for each coated specimen. To investigate the phases present in the coatings, x-ray diffraction (XRD) patterns for coatings were obtained using a BRUKER D-8 ADVANCE x-ray diffractometer with a copper target. Surface roughness values for both
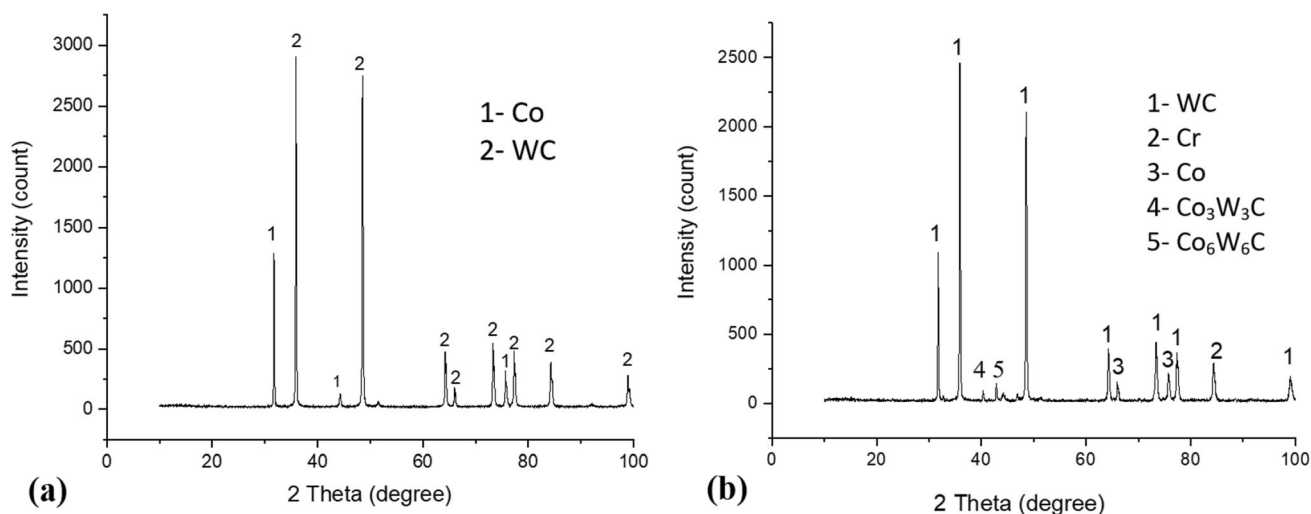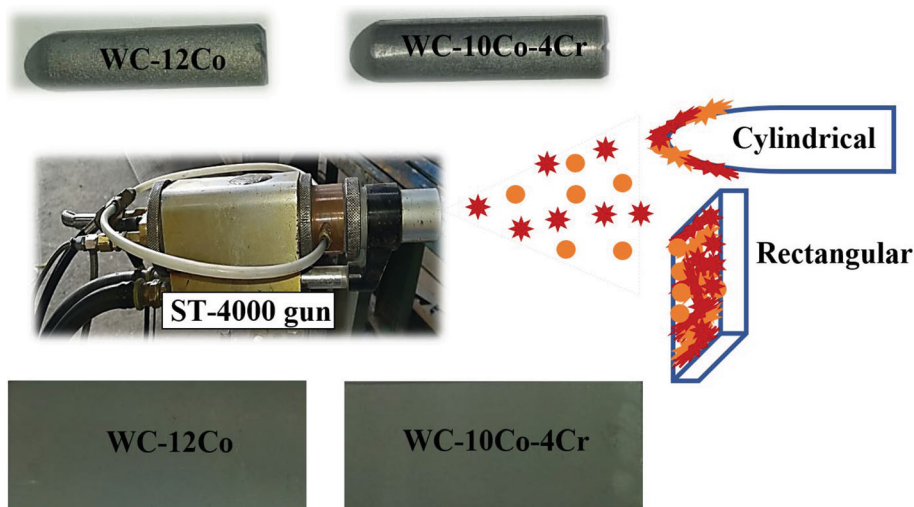
**Fig. 2** XRD images of (a) WC-12Co and (b) WC-10Co-4Cr powders



**Fig. 3** Schematic representation of HVOF coating and coated cylindrical and rectangular samples

coated and uncoated samples were measured using a surface roughness tester (Surtronic, Taylor Hobson: SE1200). Surface roughness was quantified by evaluating average Ra values at ten different locations on the surface of coated specimens, each with a gauge length of 5 mm. Microhardness and indentation fracture toughness of the coated and uncoated samples were assessed using a computerized Vickers hardness tester (RMHT-201 by Radical Scientific Equipment Private Limited, India). A load of 1000 g was applied for a duration of 20 s, and the average of ten readings was calculated for each specimen. Further, for indentation fracture toughness following equation has been used:

$$KIC = \left( E / \{ 1 - v^2 \} \right) \times \left( P / \left( c^{3/2} \right) \right)$$

where 'v' is the Poisson's ratio of the material, 'E' is the elastic modulus of the material, 'c' is the crack length, and 'P' is load (Ref 37). Also, in order to evaluate the uniformity of the coating composition and detect any potential elemental segregation or impurities, a comprehensive cross-sectional mapping of the coating was also carried out. Furthermore, SEM images of the eroded portions of both coated and uncoated specimens were obtained and analyzed to determine the wear mechanisms (Ref 35).

## Wear Testing

### Slurry Abrasion

To conduct the slurry abrasion test on both coated and uncoated specimens, a slurry abrasion test rig (DUCOM TR-44-M2) was employed. This test rig, as depicted in Fig. 4, comprises a slurry hopper positioned at the top for introducing the slurry mixture (composed of water and

**Fig. 4** Slurry abrasion test rig (DUCOM TR-44-M2)
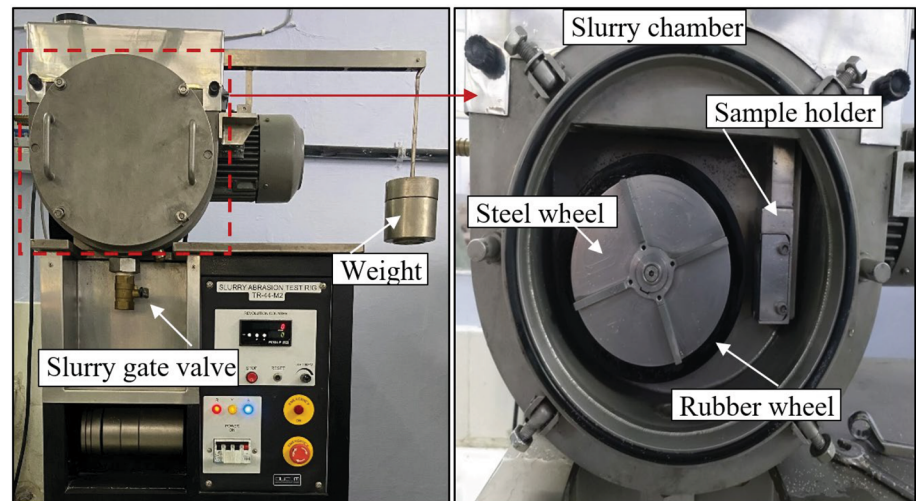


sand) into the slurry chamber. The slurry chamber is equipped with a rubber-coated steel wheel that engages with the specimen, securely held in the specimen holder. To ensure the necessary contact between the wheel and the specimen, a variable load was manually applied through an attached arm. The wheel, while fully immersed in the slurry, rotates at a controlled speed, facilitating the abrasion process. The rotational speed (RPM) of the wheel was kept consistent for each specimen, while other variables such as load (kg) and slurry concentration (ppm) were varied, ranging from 5 to 15 kg and 15000 to 45000 ppm, respectively. To dispose of the used slurry mixture, rubber debris, and burrs from eroded specimens, a slurry exit valve was incorporated, with the collected mixture directed into a vessel at the bottom of the test rig. Fresh slurry was used for each experimental run, and the test duration was set at 60 minutes. The specimens underwent a thorough cleaning process with acetone and were dried both before and after the slurry abrasion test. The mass of each specimen was meticulously measured using an electronic microbalance, with a least count of 0.1 mg. As suggested by the existing literature, the key parameters that significantly influence slurry abrasion testing are load and slurry concentration (Ref 38). In the present research, systematically varied these testing parameters for the slurry abrasion tests conducted on coated and uncoated specimens. The selected variables and their corresponding levels were developed with the help of full factorial design and the same are presented in Table 4. For the authenticity of the results, testing has been carried out thrice for each set of factor and level. Also, the sand particles utilized in the slurry abrasion tests were sourced from various fields within the Sangrur district of Punjab, India. This selection aimed to replicate the authentic field conditions encountered during the testing. Initially, the collected sand was allowed to dry naturally under the sun. Subsequently, it

**Table 4** Experimental runs as per full factorial design for slurry abrasion test

| Run | Applied Load, N | Slurry concentration, ppm |
|-----|-----------------|---------------------------|
| 1 | 5 | 15000 |
| 2 | 5 | 30000 |
| 3 | 5 | 45000 |
| 4 | 10 | 15000 |
| 5 | 10 | 30000 |
| 6 | 10 | 45000 |
| 7 | 15 | 15000 |
| 8 | 15 | 30000 |
| 9 | 15 | 45000 |

underwent sieving with a vibratory sand siever to acquire the particle size distribution (PSD). The sand particles with size more than 500 μm were discarded to mimic the original field conditions accurately. After analysis, the sand particles were observed to have particle size varying from 50-500 μm with average size as 385 μm and hardness of sand particles was observed to be $1093 \pm 8$ HV. Further, SEM image revealed that the observed sand particles exhibited a sharp and irregular morphology (as shown in Fig. 5a). Further EDS analysis disclosed that $SiO_2$ is present majorly in the sand particles (refer Fig. 5b).

*Dry Sliding*

To determine the coefficient of friction and resistance to two-body abrasion, the dry sliding tests for coated and uncoated specimens were performed using a pin-on-disk tribometer (TR-20LE-PHM-400, Ducom Instruments Pvt Ltd., India), as shown in Fig. 6, in accordance with the standard ASTM-G99-17 (Ref 39). An EN31 disk of
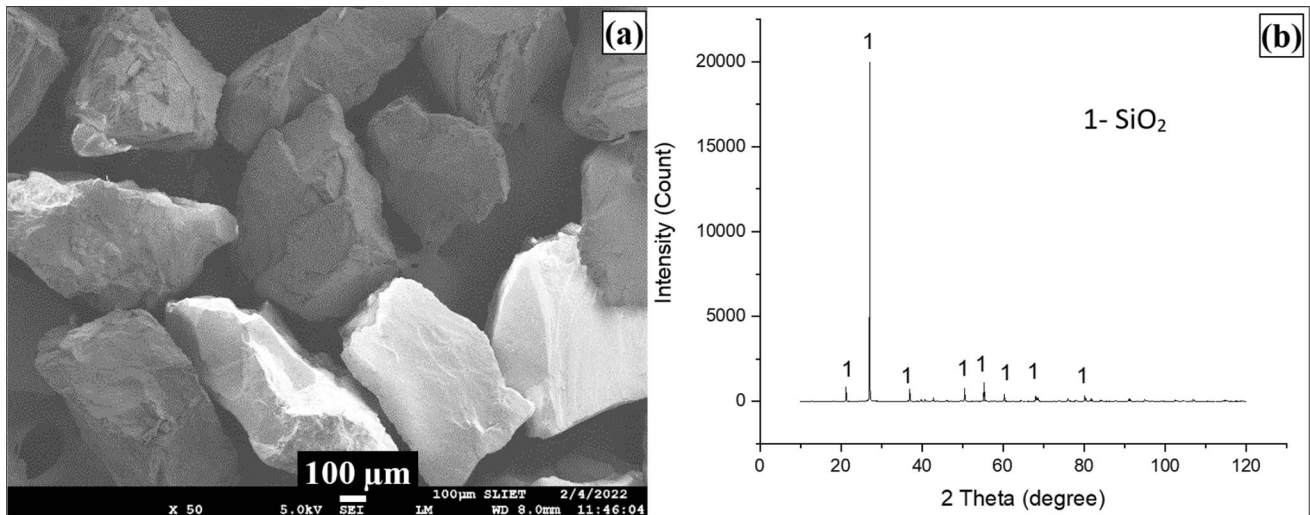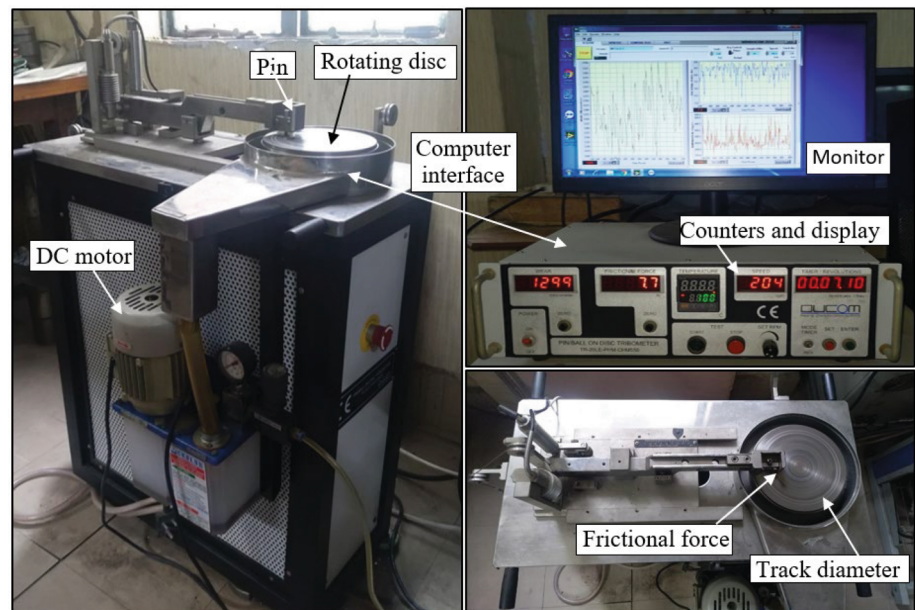
**Fig. 5** (a) SEM and (b) EDS analysis of erodent (sand) particles

**Fig. 6** Pin-on-disk tribometer (TR-20LE-PHM-400, Ducom Instruments Pvt Ltd., India)



hardness HRC 60 and surface roughness of Ra 0.05 μm with diameter and thickness 165 and 8 mm, respectively, have been taken into consideration. The pin of 8 mm diameter, as illustrated in Fig. 3, was positioned perpendicular to the EN31 disk during the tests to evaluate the behavior of as-deposited coatings, without additional grinding or polishing against sliding situation, for simulating real-world conditions where coatings may be subjected to wear without prior surface treatment. In order to thoroughly analyze the performance of the coatings, a comprehensive experimental framework was employed. This involved varying two critical factors, namely applied load and disk rotation speed (rpm), with each factor examined across three different levels. This systematic

approach resulted in nine experimental runs, each representing a distinct combination of load and rpm (refer Table 5). Other operating parameters were maintained at the same level, including a rotation diameter of 4 cm and a test duration of 10 minutes. For the authenticity of the results, each experiment has been conducted thrice for each set of experimental runs as presented in Table 5.

The coefficient of friction was determined with the assistance of proximity and load sensors attached to the tribometer. The measurement of wear was carried out by calculating the mass loss, which involved measuring the initial and final mass of the pins using an electronic weighing machine with a precision of 0.01 mg. Furthermore, the mass loss rate $(\dot{m})$ (gm/Nm) for each pin

**Table 5** Experimental runs as per full factorial design for dry sliding test

| Run | Applied load, N | Rotation speed, rpm |
|---|---|---|
| 1 | 20 | 100 |
| 2 | 20 | 200 |
| 3 | 20 | 300 |
| 4 | 40 | 100 |
| 5 | 40 | 200 |
| 6 | 40 | 300 |
| 7 | 60 | 100 |
| 8 | 60 | 200 |
| 9 | 60 | 300 |

specimen was calculated using the mass loss ($\triangle$m) (gm), the applied load (P) (N), the sliding velocity (v) (m/s), and the test duration (t) (s) values. This calculation was performed using the expression $\dot{m} = (\triangle m)/(P.v.t)$ (Ref 40). For each specified specimen, five replicates were taken for analysis, and the average values of the mass loss rate and coefficient of friction were determined for comparison. Moreover, to understand the mechanisms behind the variations in wear, scanning electron microscopy (SEM) was utilized to examine the worn-out surfaces of the specimens at the harshest conditions. This provided insights into the factors contributing to differences in wear behavior.
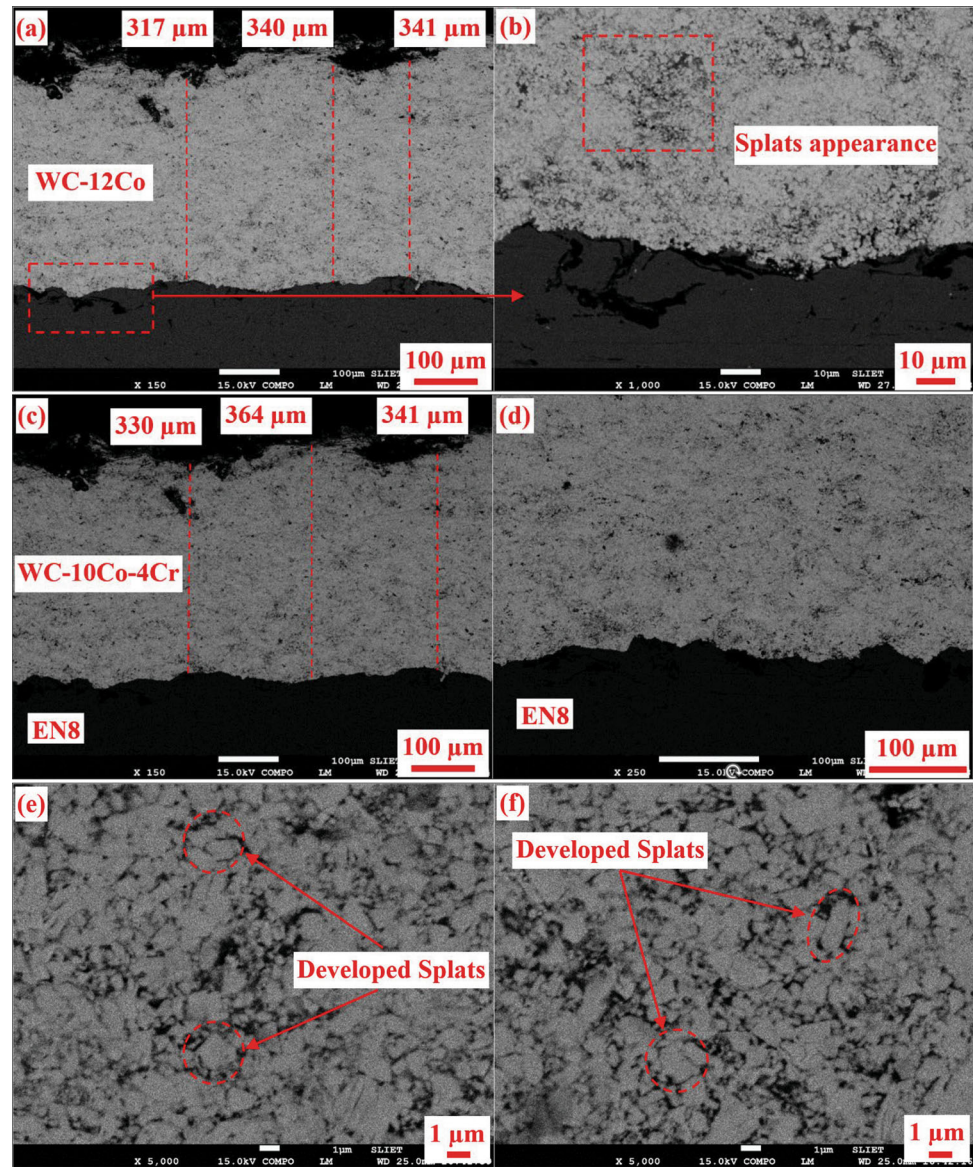
## Results and Discussions

### Metallurgical Characterization

The cross-sectional examination of the coated specimens, which included two distinct compositions, WC-12Co and WC-10Co-4Cr, was performed using field-emission scanning electron microscopy (FESEM) with the JSM-7610F-plus instrument from JEOL, Japan. The cross-sectional SEM images of these coatings are featured in Fig. 7(a), (b) (c), and (d), respectively. These images unveiled a noteworthy similarity in their splat-like microstructure, a hallmark attribute associated with HVOF coatings, as substantiated by prior literature (Ref 40). Notably, both the coatings exhibited a compact structure with robust cohesion to the substrate. In the case of coating WC-12Co, as evidenced in Figure 7 (a), and (b), the cross section showcased a combination of partially/unmelted and fully melted WC-12Co particles, resulting in the presence of residual pores distributed throughout the coating cross section. Conversely, WC-10Co-4Cr coating, as depicted in Fig. 7 (c), and (d), displayed more occurrence of voids and pores compared to coating WC-12Co. This might have

occurred owing to the diverse distribution of the binder within the coatings. In WC-12Co, the cobalt binder may be uniformly distributed, promoting better cohesion, and reducing porosity. In contrast, WC-10Co-4Cr may exhibit a less uniform distribution of the binder, which can lead to variations in porosity. Further, the unique melting characteristics of each coating material can substantially impact the microstructural properties. The introduction of chromium in WC-10Co-4Cr might have influenced the behavior of the coating material during melting, potentially resulting in the formation of more pores and contributing to differences in coating thickness. Also, it was evident that each of the candidate coatings exhibited distinct yet consistently uniform thickness across their cross sections. The microstructure of the samples was also analyzed, revealing the presence of splats on the surface of the high-velocity oxygen fuel (HVOF) sprayed samples, as shown in Fig. 7 (e) and (f). The formation of splats on the surface of the HVOF-sprayed samples may have occurred due to several factors. During the HVOF spraying process, powder particles are accelerated to high velocities and impact the substrate with significant kinetic energy. This impact likely caused the particles to flatten and spread upon contact with the substrate, forming splats. Additionally, the elevated temperatures experienced by both the substrate and the powder particles during spraying might have facilitated the partial melting and deformation of the powder particles upon impact, contributing to the formation of flattened splats on the substrate surface. Moreover, the microstructure and composition of the coating material could have influenced the morphology of the splats formed during the spraying process. Variations in material properties, such as hardness, melting point, and particle size distribution, might have influenced how the powder particles deformed upon impact, leading to differences in splat morphology.

In the context of elemental mapping, an in-depth exploration of the elemental composition and distribution within both WC-12Co and WC-10Co-4Cr coatings was executed using energy-dispersive x-ray spectroscopy (EDS) mapping (refer Fig. 8 and 9). This analytical process yielded crucial insights into the spatial arrangement of key elements within the coatings. The elemental mapping revealed a notable outcome: a consistent and uniform dispersion of elements across the coatings. The mapping observations unequivocally demonstrated that elements such as tungsten (W), cobalt (Co), and chromium (Cr) were uniformly distributed throughout the cross sections of both coatings. This uniformity extended to the presence of other elemental components, including carbon (C) and iron (Fe), confirming their consistent dispersion. This uniform dispersion of elements is a significant finding, as it indicates that these coatings exhibit consistent and reliable elemental

**Fig. 7** Cross-sectional SEM images of (a-b) Coating WC-12Co, (c-d) Coating WC-10Co-4Cr, and (e-f) Splat formation analysis of coated surface



## XRD Analysis

X-ray diffraction (XRD) analysis plays a pivotal role in elucidating the crystalline phases present within WC-12Co and WC-10Co-4Cr coatings, providing a deeper understanding of their structural composition. Some distinct crystalline phases were discerned in XRD pattern of WC-12Co coating (refer Fig. 10a), namely WC, W, and Co. WC was expected in the coating as it is the fundamental component renowned for its exceptional hardness and wear resistance, making it crucial for tribological applications. The presence of sharp diffraction peaks corresponding to WC in the XRD pattern corroborated its existence (refer

composition, which can significantly impact their mechanical and tribological properties (refer Fig. 8 and 9).

Fig. 10a). Secondly, decarburized phase such as $W_2C$ and ternary phase as $Co_6W_6C$ was also found to be present in the WC-12Co coating. Its presence suggests a complex interplay of carbon (C) and cobalt (Co) within the coating material. Also, similar to WC-12Co coating, in WC-10Co-4Cr coating major peaks corresponding to WC, along with decarburized phase, such as $W_2C$ was also found. In contrast, due to presence of Cr, XRD pattern for WC-10Co-4Cr (refer Fig. 10b) unveiled a more intricate landscape, with the detection of some distinct crystalline phases, namely $C_2Cr_3$ and $CoCr_2$ were also found. Again, the WC was strongly expected in the coating as it is the fundamental component, but the presence of $C_2Cr_3$ and $CoCr_2$ signifies the incorporation of chromium (Cr) into the coating, enhancing hardness and corrosion resistance. This attribute is valuable for durability in challenging
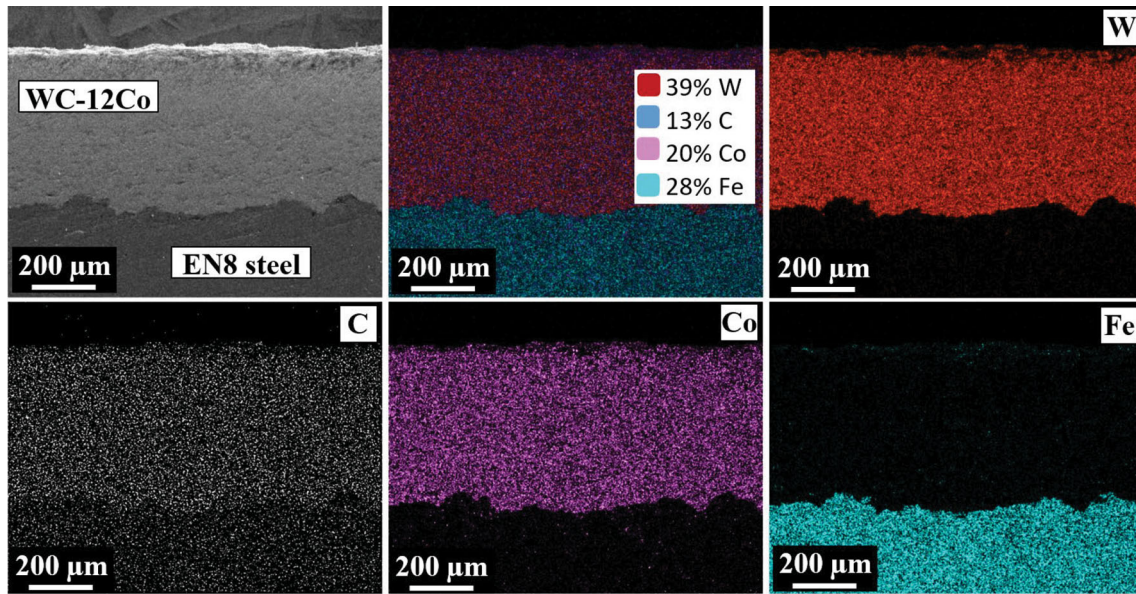
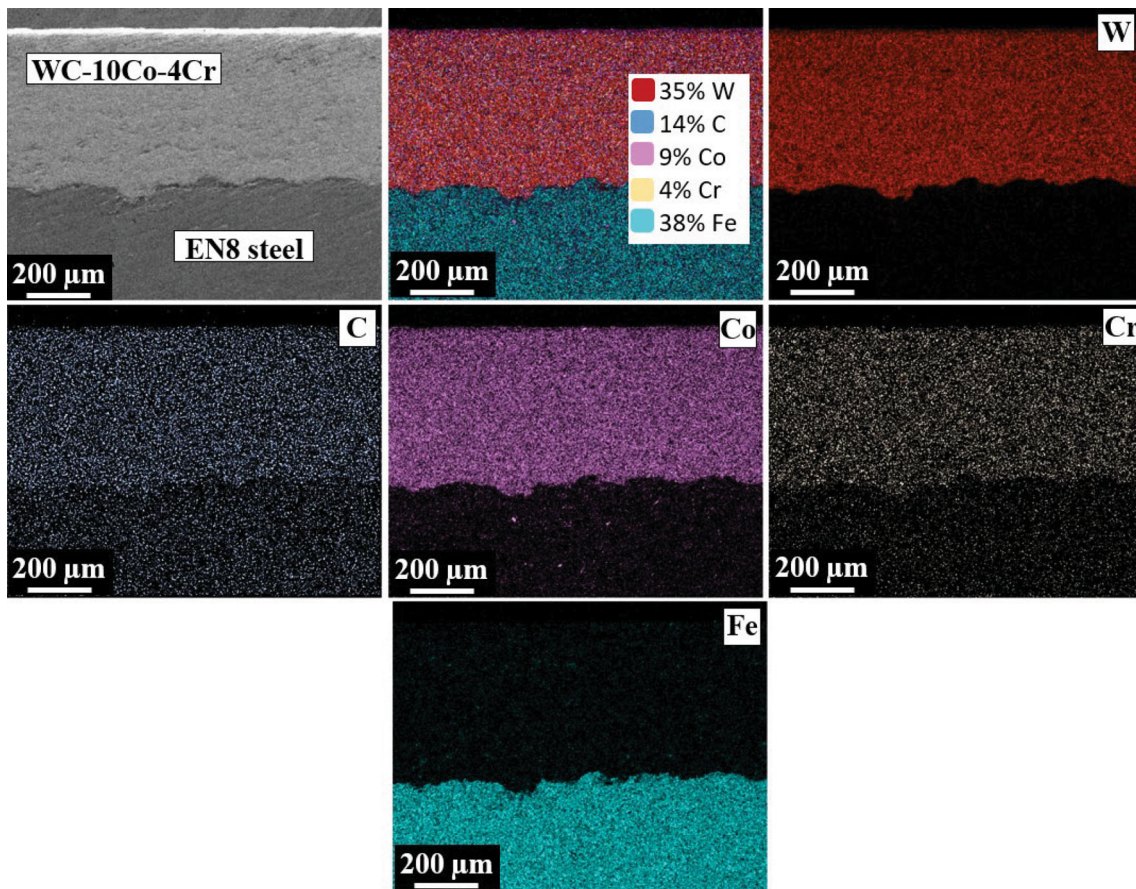**Fig. 8** Cross-sectional EDS mapping of coating WC-12Co



**Fig. 9** Cross-sectional EDS mapping of coating WC-10Co-4Cr

environments. Further, the appearance of a cobalt-chromium alloy (Co/Cr) phase points to the alloying of cobalt and chromium within the coating was observed. Such an alloy has the potential to enhance mechanical properties, including hardness and toughness. The presence of these distinct crystalline phases in both coatings underscores the
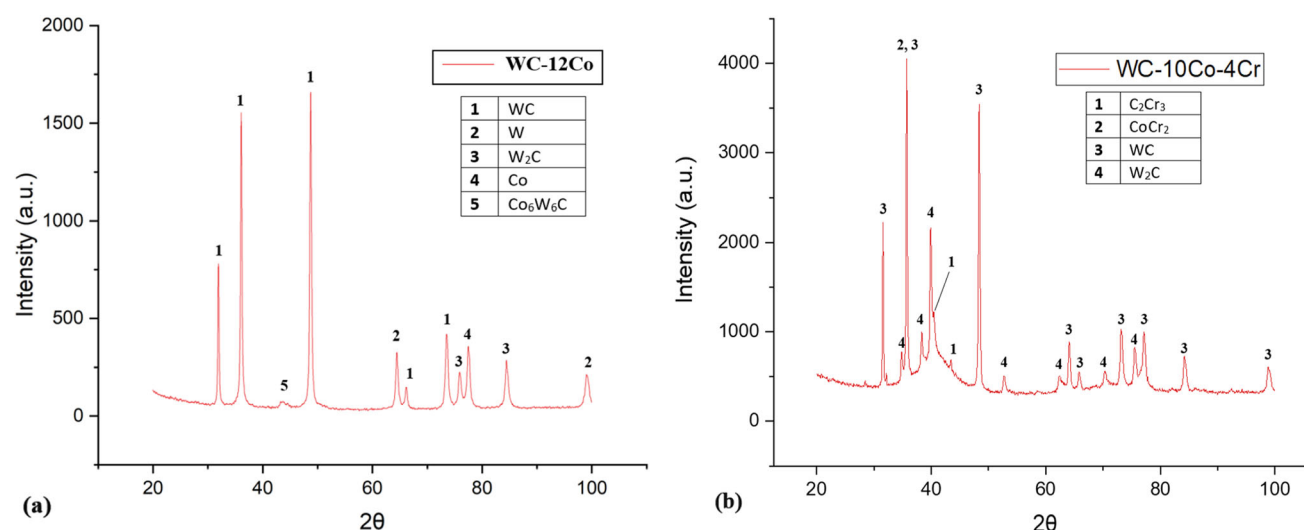
**Fig. 10** XRD patterns for (a) WC-12Co, (b) WC-10Co-4Cr

intricate interplay of elements within their compositions. The detailed insights including PDF database number/ JCPDF number/COD, miller indices, and d-spacing values of all the phases present in the coating are shown in Table 6 for reference.

## Mechanical Characterization

WC-12Co exhibited notably lower porosity % than that of coating WC-10Co-4Cr (refer Fig. 11). This disparity in average porosity can be attributed to variations in the coating compositions. Coating WC-12Co, with its composition, may have facilitated a more compact and denser microstructure, resulting in fewer voids or pores. On the other hand, coating WC-10Co-4Cr, with its distinct composition, could have led to the presence of a higher volume of voids, affecting its average porosity %. In favor of this, coating WC-12Co (332 μm) displayed a significantly less coating thickness than that of coating WC-10Co-4Cr (345 μm). This relationship between average porosity and coating thickness has been attributed to the density and compactness of the coatings. A decrease in average porosity in WC-12Co suggested a denser microstructure, resulting in a thinner coating. Conversely, the higher average porosity in WC-10Co-4Cr implies a less compact structure, leading to a thicker coating.

Also, coating WC-12Co exhibited a microhardness of 964 HV, which was lower than that of coating WC-10Co-4Cr, with a microhardness of 1012 HV. These differences in microhardness can be attributed to the material compositions. WC-10Co-4Cr, with its unique blend of elements, likely exhibited enhanced hardness, resulting in a higher microhardness value. Conversely, WC-12Co composition may have rendered it less resistant to plastic

deformation, leading to a lower microhardness. Also, the microhardness for the EN8 steel was observed to be 218 HV which is comparatively on the lower side as when compared with coated samples. Further, coating WC-12Co displayed an indentation fracture toughness of 7.1 MPa.m$^{1/2}$, which was lower than that of coating WC-10Co-4Cr, with an indentation fracture toughness of 7.4 MPa.m$^{1/2}$. This might have occurred owing to the fact that WC-10Co-4Cr composition likely conferred greater resistance to crack propagation, resulting in a higher fracture toughness. Also, the indentation fracture toughness for the EN8 steel was observed to be higher with an average value of 34 MPa.m$^{1/2}$. In contrast, WC-12Co composition may have rendered it more susceptible to crack initiation and propagation. Surface roughness quantifies the irregularities on a material's surface. Coating WC-12Co exhibited a surface roughness with an average Ra value of 3.966 μm, which was lower than that of coating WC-10Co-4Cr, with an average Ra value of 4.736 μm. Coating WC-12Co, with its composition and deposition characteristics, likely resulted in a smoother surface with fewer irregularities. Conversely, WC-10Co-4Cr's unique attributes could have led to a slightly rougher surface. This variation in surface roughness was also observed to be aligned with the porosity % variations of the coating.

## Slurry Abrasion Wear Studies

The effect of various factors on slurry abrasion testing has been analyzed by full factorial method as summarized in Section "Wear Testing". The results of the slurry abrasion test are presented in Fig. 12.

From the results, it was observed that mass loss has been increased with the increase in load and slurry

**Table 6** PDF database number, miller indices, and d-spacing corresponding to different phases obtained for both coatings.

| Sr. No. | 2Θ, degree | Phase | Miller indices | D spacing, nm | COD/ JCPDF |
|---|---|---|---|---|---|
| HVOF-sprayed WC-12Co Coating | | | | | |
| 1 | 35.697 | WC | $(\bar{1}\,0\,0)$ | 2.513 | 9013303 |
| 2 | 37.578 | WC | $(0\,0\,\bar{1})$ | 2.831 | 9013303 |
| 3 | 44.62 | $Co_6W_6C$ | $(3\,3\,1)$ | 2.141 | 23-0939 |
| 4 | 48.39 | WC | $(\bar{1}\,0\,\bar{1})$ | 1.8795 | 9013303 |
| 5 | 64.91 | W | $(\overline{2\,2}\,0)$ | 1.4354 | 1534935 |
| 6 | 65.93 | WC | $(0\,0\,2)$ | 1.4155 | 9013303 |
| 7 | 73.24 | WC | $(\bar{2}\,1\,\bar{1})$ | 1.2913 | 9013303 |
| 8 | 75.998 | $W_2C$ | $(\bar{4}\,2\,1)$ | 1.25 | 1539792/35-776 |
| 9 | 77.84 | Co | $(2\,2\,0)$ | 2.11 | 00-015-0806 |
| 10 | 85.27 | $W_2C$ | $(\bar{4}\,2\,\bar{2})$ | 1.1372 | 1539792/35-776 |
| 11 | 99.441 | W | $(\overline{3\,1}\,0)$ | 1.0097 | 1512550 |
| HVOF-sprayed WC-10Co-4Cr Coating | | | | | |
| 1 | 31.578 | WC | $(0\,0\,\bar{1}))$ | 2.8310 | 9013303 |
| 2 | 34.536 | $W_2C$ | $(\bar{2}1\,0)$ | 2.595 | 1539792/35-776 |
| 3 | 35.69 | WC | $(\bar{1}\,0\,0)$ | 2.513 | 9013303 |
| 4 | 35.69 | $CoCr_2$ | $(3\,\bar{1}\,\bar{1})$ | 2.513 | 1538331 |
| 5 | 38.067 | $W_2C$ | $(0\,0\,\bar{2}))$ | 2.362 | 1539792/35-776 |
| 6 | 39.593 | $W_2C$ | $(\bar{2}1\,0)$ | 2.274 | 1539792/35-776 |
| 7 | 40.280 | $C_2Cr_3$ | $(2\,0\,\bar{3})$ | 2.237 | 1540070/35-804 |
| 8 | 43.620 | $C_2Cr_3$ | $(\bar{1}\,\bar{1}\,\bar{1})$ | 2.073 | 1540070/35-804 |
| 9 | 48.39 | WC | $(\bar{1}\,0\,\bar{1})$ | 1.8795 | 9013303 |
| 10 | 52.333 | $W_2C$ | $(\bar{2}12)$ | 1.746 | 1539792/35-776 |
| 11 | 61.881 | $W_2C$ | $(\bar{3}00)$ | 1.498 | 1539792/35-776 |
| 12 | 64.129 | WC | $(\bar{2}1\,0)$ | 1.451 | 9013303 |
| 13 | 65.93 | WC | $(0\,0\,2)$ | 1.4155 | 9013303 |
| 14 | 72.837 | $W_2C$ | $(\bar{4}2\,0)$ | 1.297 | 1539792/35-776 |
| 15 | 73.24 | WC | $(\bar{2}\,1\,\bar{1})$ | 1.2913 | 9013303 |
| 16 | 75.011 | $W_2C$ | $(\bar{3}\,0\,\bar{2})$ | 1.265 | 1539792/35-776 |
| 17 | 77.303 | WC | $(\bar{1}\,0\,\bar{2})$ | 1.233 | 9013303 |
| 18 | 84.242 | WC | $(\bar{2}\,0\,\bar{1})$ | 1.148 | 9013303 |
| 19 | 98.975 | WC | $(\bar{2}\,1\,\bar{2})$ | 1.013 | 9013303 |
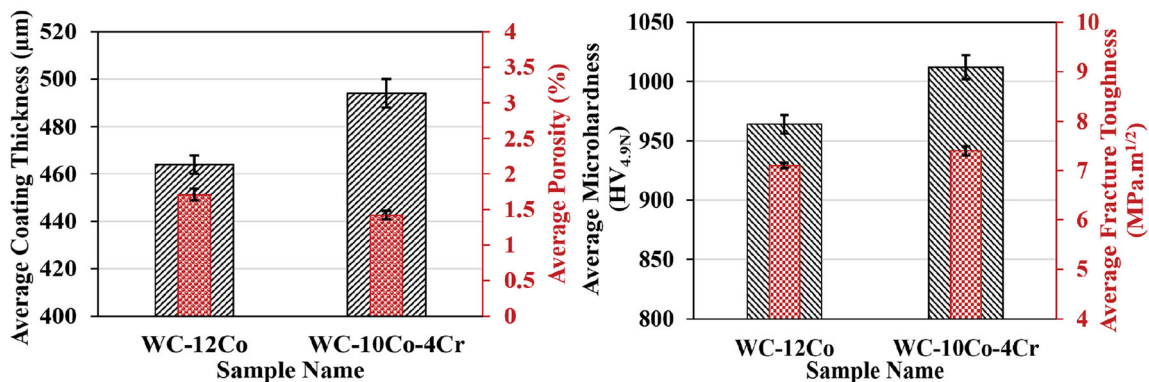


**Fig. 11** Average coating thickness, porosity %, microhardness, and indentation fracture toughness data of HVOF coated WC-10Co-4Cr and WC-12Co
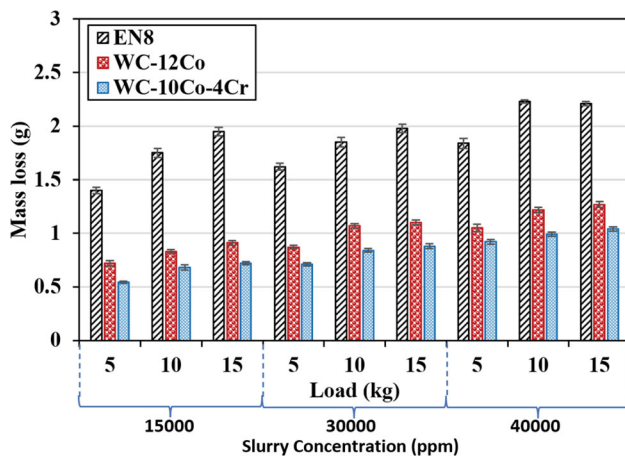
Fig. 12 Average mass loss of the EN8 and HVOF coated WC-10Co-4Cr and WC-12Co specimens under variable conditions of slurry abrasion wear
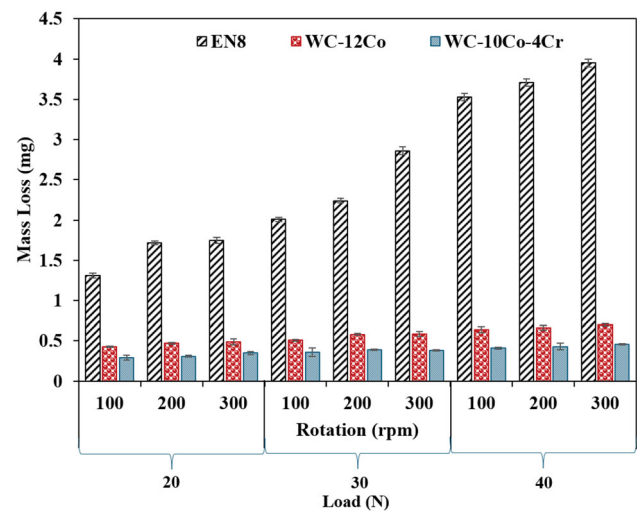


Fig. 13 Average mass loss of the EN8 and HVOF coated WC-10Co-4Cr and WC-12Co specimen under variable condition of dry sliding wear
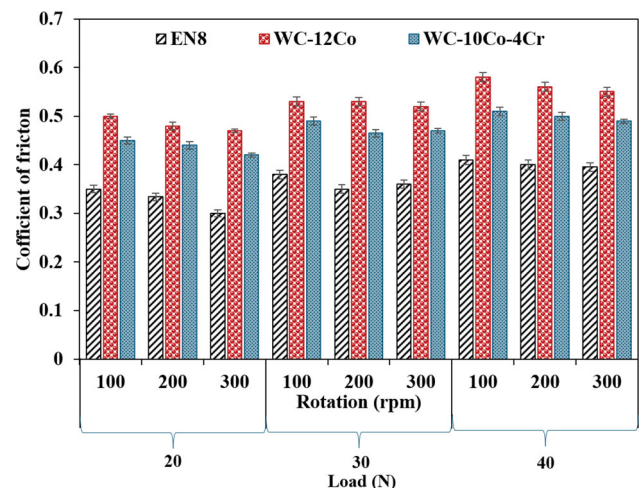


Fig. 14 Coefficient of friction of the EN8 and HVOF coated WC-10Co-4Cr and WC-12Co specimen under variable condition of dry sliding wear

concentration. This might have occurred owing to, increased contact pressures and forces experienced by the specimens (coated and uncoated). As the load intensified, it might have exerted a greater stress on the materials, potentially leading to more pronounced wear and material removal. Further, the parallel escalation in mass loss with rising slurry concentration has been a consequence of the abrasive nature of the slurry itself. A denser slurry concentration implies a greater abundance of abrasive particles suspended in the liquid medium. These particles, in turn, become more effective agents of wear. The increased concentration augments the abrasive action, thereby contributed to the elevated mass loss. Moreover, in the case of coated and uncoated specimens, coated specimens had shown good wear resistance as compared to the uncoated specimens. This could have occurred owing to the higher hardness and indentation fracture toughness of the coating particles. It can also be said that softer and ductile nature of EN8 steel has been found to be more likely to slurry abrasion. The same finding has also been observed in the existing literature.

### Dry Sliding Wear Studies

The effect of various factors on dry sliding testing has been analyzed by full factorial method as summarized in Section "Wear Testing". The insights gained from the pin-on-disk tests are revealed through Fig. 13 and 14, presenting the average mass loss and coefficient of friction values, respectively, for coated and uncoated samples.

All tests strictly adhered to the protocols outlined in Section "Slurry Abrasion". The results of the pin-on-disk tests revealed that the EN8 steel exhibits a significantly lower resistance to two-body abrasion, with a mass loss rate a staggering 3 times higher than the coated surfaces.

This finding aligns with the observed trends in hardness and indentation fracture toughness as detailed in Section "Mechanical Characterization". It is worth noting that the inverse relationship between hardness/indentation fracture toughness and mass loss rate plays a pivotal role in this context, as the wear resistance of coated samples is intrinsically tied to their higher hardness and fracture toughness.

The base steel, composed of EN8 steel, is marked by its ductile and soft nature. In contrast, the coated surfaces exhibit greater hardness, which bestows them with heightened wear resistance. When subjected to abrasion, the base steel may undergo plastic distortion or detachment, potentially leading to the aggregation of debris between the sliding surfaces. This phenomenon, in turn,

contributes to the higher mass loss rate observed in the base steel. Additionally, the coated specimens tell a distinct tale. WC-10Co-4Cr, being harder owing to the presence of tungsten carbide, had shown less interaction between the harder tungsten carbide particles and the disk surface. These hard particles might plow into the disk material, causing abrasion and material removal. The cobalt matrix in the coating might have helped in maintaining the cohesion of the tungsten carbide particles, preventing their detachment, and leading to more controlled abrasive wear. Figure 14 also offers insights into the average coefficient of friction, highlighting its notable variations. The base steel exhibits the highest coefficient of friction, a likely contributor to its elevated mass loss. The presence of debris generated through plastic deformation and material extraction is indeed substantiated by the higher coefficient of friction in the case of the base steel. Conversely, the coated samples showcase an intriguing contrast in their coefficient of friction trends. WC-10Co-4Cr notably, showed the lowest coefficient of friction, attributed to its exceptionally hardness and scattered surface roughness. In contrast, WC-12Co showed less value as compared with WC-10Co-4Cr owing to the comparatively less hardness. Moreover, it can be said in both the coated specimen surfaces that the dispersion of WC particles within the local vicinity of the top layer might have diminished the smoothness, resulting in higher coefficient of friction values. However, this increase in friction coefficients does not translate into elevated mass loss, thanks to the substantial support provided by the hard WC particles.

## Slurry Wear Mechanism

SEM analysis was conducted on the specimens after dry sliding and slurry abrasion testing using FESEM (JSM-7610Fplus, JEOL, Japan). The analysis of SEM images revealed that the specimens exhibited varying degrees of degradation, which were influenced by their respective ductile or brittle nature. The following subsections present the after-testing slurry wear mechanism of the coated and uncoated samples:

### After Slurry Abrasion Testing

Wear signatures including material abrading, material displacement caused by abrasive action, microcuts, and evidence of ductile failure (refer Fig. 15a) are observed over EN8 steel specimen after slurry abrasion testing at the harshest condition. Material abrading has been a consequence of the abrasive action of the slurry, leading to the gradual removal of material from the surface. The material displacement caused by abrasive action indicates the digging effect of abrasive particles on the softer material,

caused localized material displacement. Microcuts have been resulted owing to the abrasive particles plowing through the surface, creating small channels or grooves. Ductile failure was evident as localized plastic deformation in the form of grooves or depressions. These signatures collectively reflect the abrasive wear mechanism during slurry abrasion testing, where the abrasive particles cause material removal, plastic deformation, and the formation of characteristic surface features over EN8 steel. Further, distinct wear signatures such as cut marks, cavities, chipping of material, and deep grooves are observed on the surface of both the HVOF coated specimens (refer Fig. 15b and c). These features might have been attributed to the abrasive action of the slurry and the interaction between the coating and abrasive particles. Cut marks might have been formed as abrasive particles plow through the surface, leaving distinctive tracks. Cavities are likely to be formed as a result of localized material removal and slurry wear caused by the high-stress environment. Chipping of material could have been occurred when the abrasive forces exceed the coating's adhesive strength, leading to the detachment of small fragments. Deep grooves have been indicative of significant material loss due to the abrasive wear. Overall, it can be deduced that EN8 steel has primarily shown the ductile mode of failure, and coated specimens have shown the brittle mode of failure. Similar types of observations have also been observed in the existing literature (Ref 41).

### After Dry Sliding Testing (Pin-on-Disk)

Distinct wear signatures such as abrasive chipping, deformed material debris, ductile failure, and the presence of cavities and pores are observed on the worn surfaces of EN8 steel (refer Fig. 16a). These features are primarily attributed to the material's relatively softer and more ductile nature when subjected to the abrasive action and high contact pressures exerted during the testing. Abrasive chipping might have resulted from the plowing and abrasive forces applied by harder counterparts, leading to the detachment of small fragments. Deformed material debris might have been generated through plastic deformation of the material under the applied load. Ductile failure has been observed as localized plastic deformation, typically in the form of grooves or depressions. Further, the presence of inherent cavities and pores in the material exacerbates wear by acting as sites for stress concentration and material removal. Collectively, these signatures indicate that abrasive wear and plastic deformation are the predominant wear mechanisms in EN8 steel during pin-on-disk testing. Next, in the case of WC-10Co-4Cr and WC-12Co coating, similar type of signatures was observed including deformed and spattered material, roughening of HVOF splats,
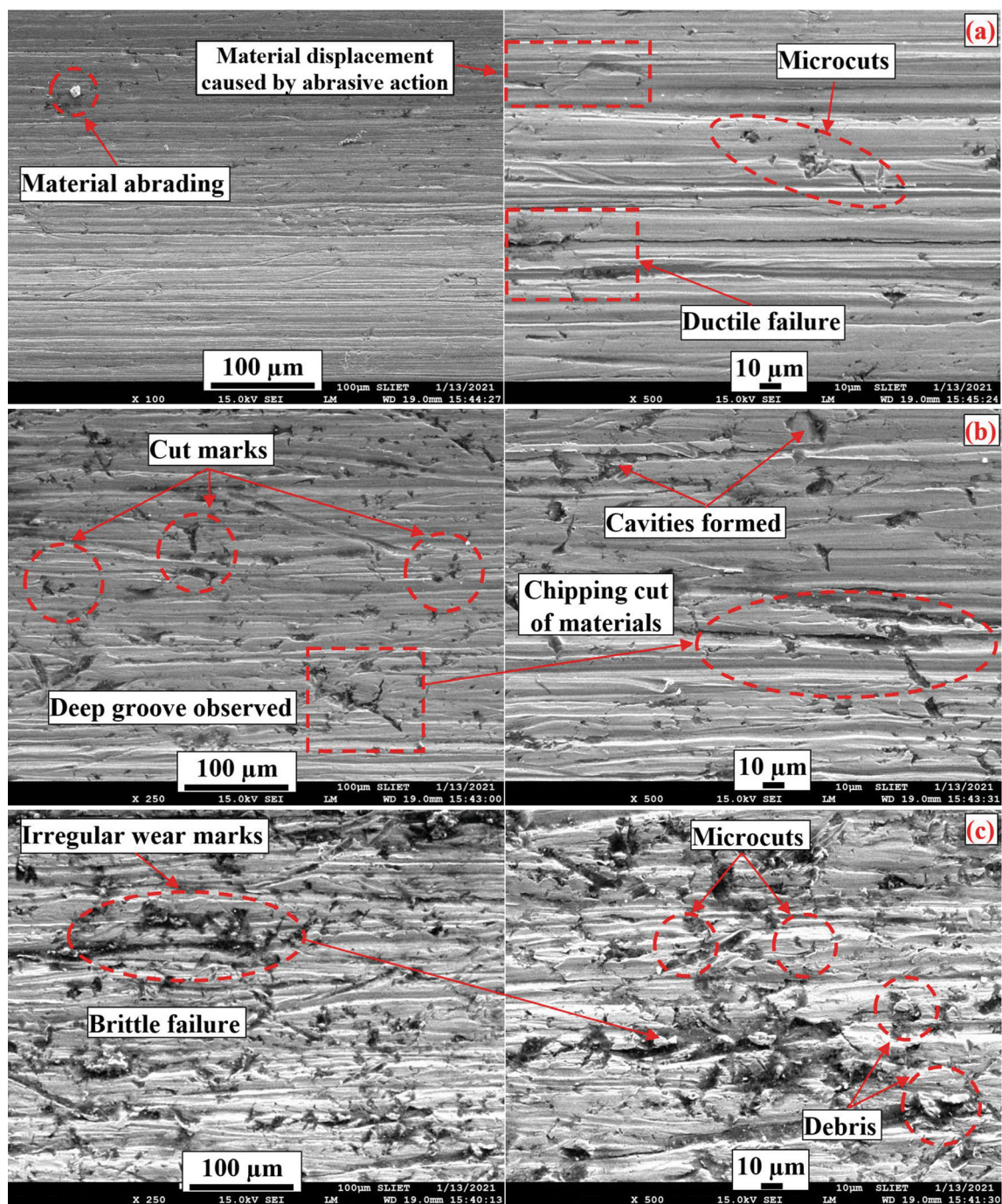
**Fig. 15** SEM images of eroded surfaces of (a) EN8 steel, (b) WC-10Co-4Cr, and (c) WC-12Co at the harshest conditions after slurry abrasion testing

material flow, and the presence of micropores are found to be observed (refer Fig. 16b, and c). Deformed and spattered material might have been occurred due to the high contact pressures and abrasive forces during the testing, leading to the ejection of small splatter particles from the coating. Roughening of HVOF splats results from the abrasive action and wear at the surface of individual splats;

however, the mechanical interaction with the counterpart (EN31 disk) roughens the splats. Material flow has been observed as a result of the mechanical interaction between the coating and the counterpart, which causes the material to flow and redistribute on the surface. Moreover, micropores are likely formed during the HVOF spraying process due to the entrapment of air or gas within the coating
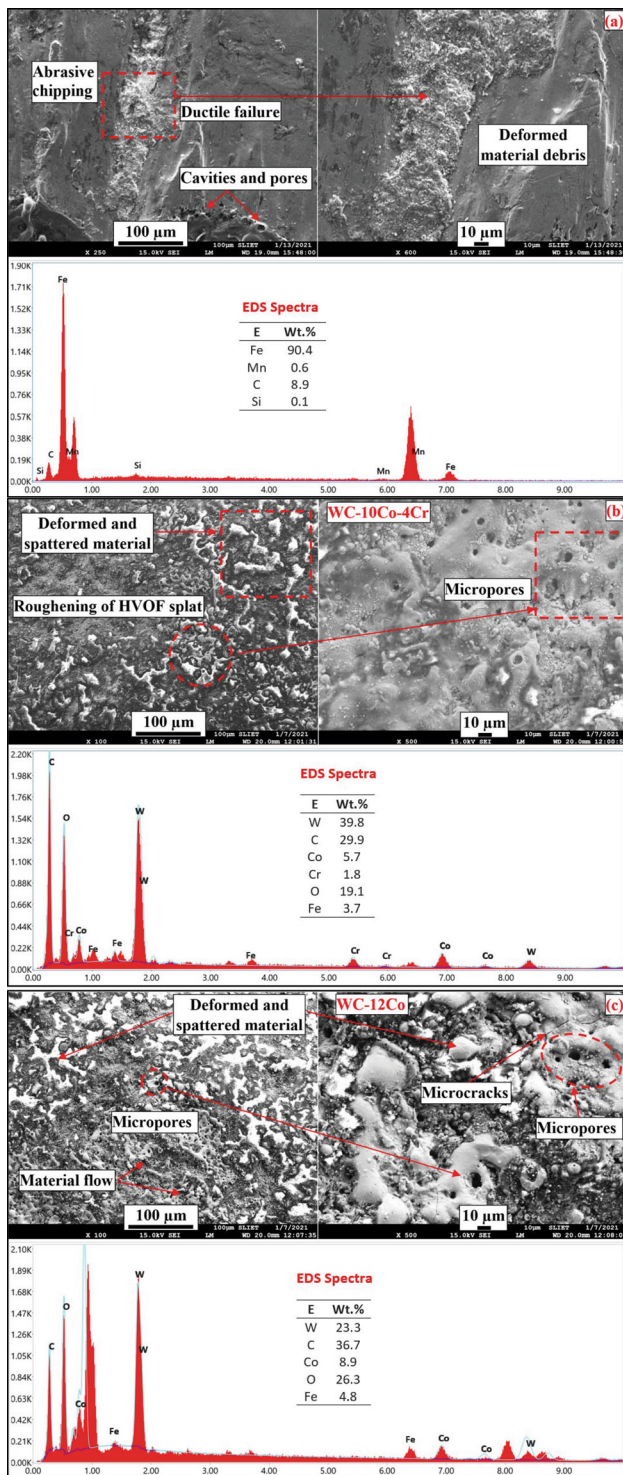
**Fig. 16** SEM images and EDS spectra of worn-out surfaces of (a) EN8 steel, (b) WC-10Co-4Cr, and (c) WC-12Co at the harshest conditions after dry sliding testing

material, and these pores can become stress concentration sites during wear. The other important signature was observed as smearing of transferred steel. It is likely that steel might be smeared from the softer EN31 counterpart onto the coatings, the same can also be seen in EDS spectra of both the coatings as Fe was observed in the elements (refer Fig. 16b and c), that may be accumulated into the valleys of the rough coating surface hence resulting in flatness of the coating surface. And after this, the rubbing takes place between the EN31 and flattened coating pins.

## Conclusions

In the present work, WC-10Co-4Cr and WC-12Co coating was developed using HVOF spraying process, for improving the slurry abrasion and dry sliding resistance of EN8 steel. The main findings are as follows:

1. Successful development of WC-10Co-4Cr and WC-12Co coatings using the HVOF spraying process, exhibiting a compact structure with strong adhesion to the substrate.
2. The coatings exhibited the presence of mainly tungsten (W), tungsten carbide (WC), carbon (C) along with decarburized phase such as $W_2C$ and ternary phase as confirmed x-ray diffraction (XRD) analysis. Moreover, some distinct crystalline phases, namely Cr, $C_2Cr_3$, $CoCr_2$, and $Cr_7C_3$, have also showed their existence with the addition of Cr in case of WC-10Co-4Cr coating, underscoring their properness for applications requiring enhanced wear resistance.
3. The microhardness of coated specimen was found to be 4.42 and 4.64 times for WC-12Co and WC-10Co-4Cr coating, respectively, as compared with EN8 steel. This enhancement in microhardness may be attributed to the unique composition and deposition characteristics of the coatings, which include tungsten carbide (WC), cobalt (Co), chromium (Cr), and other alloying elements. However, indentation fracture toughness is less for coated samples 79.11% and 78.23% less for WC-12Co and WC-10Co-4Cr coatings, respectively, in comparison with EN8 steel.
4. Differential performance observed in slurry abrasion and dry sliding wear tests, highlighting the coatings' effectiveness in mitigating wear under varying conditions.

5. The EN8 steel exhibited ductile wear, where material removal occurred primarily due to plastic deformation and chipping. In contrast, the coated specimens displayed brittle wear characteristics, with the detachment of splats or WC particles and contributing to wear.

# References

1. M.M. Waqas, M. Wasim, M. Ashraf, and W.N. Jatoi, Engineering Principles of Precision Farming: Pathway for the Developing Countries to Ensure Food Security, *Climate Change Impacts on Agriculture: Concepts, Issues and Policies for Developing Countries.* Springer International Publishing, Cham, 2023, p 105-133

2. B. Aramide, S. Pityana, R. Sadiku, T. Jamiru and P. Popoola, Improving the Durability of Tillage Tools Through Surface Modification—a Review, *Int. J. Adv. Manuf. Technol.*, 2021, **116**(1-2), p 83-98.

3. R.A. Lorenzi, V.V. de Castro, M. Bullmann, A.M. de Andrade, P. Mariot and M.C. de Fraga, Increased Wear Resistance of Cultivator Coulters Coated with Fe-Cr-Nb Cladding and Evaluated in Field Conditions: Sandy and Compacted Soil in Southern Brazil, *Int. J. Adv. Manuf. Technol.*, 2023, **129**(3), p 1601-1612.

4. X. Wang, H. Zhou, S. Wang, H. Zhou and J. Ji, Methods for Reducing the Tillage Force of Subsoiling Tools: A Review, *Soil Tillage Res.*, 2023, **229**, 105676.

5. M. Ucgul and C.L. Chang, Design and Application of Agricultural Equipment in Tillage Systems, *Agriculture*, 2023, **13**(4), p 790.

6. R. Kumar, S. Sharma, J.P. Singh, P. Gulati, G. Singh, S.P. Dwivedi and M. Abbas, Enhancement in Wear-Resistance of 30MNCRB5 Boron Steel-Substrate using HVOF Thermal Sprayed WC-10% Co-4% Cr Coatings: A Comprehensive Research on Microstructural, Tribological, and Morphological Analysis, *J. Mater. Res. Technol.*, 2023, **27**, p 1072-1096.

7. Tulaganova, L., Yunushuzhaev, S., & Juraeva, G. Improving the Wear Resistance and Durability of Cultivator Tools. In Journal of Physics: Conference Series (Vol. 2373, No. 2, p. 022026). IOP Publishing (2022).

8. S. Singh and S.S. Chatha, Influence of Hardfacings on Wear Behavior of EN-42A Steel in Actual Field Conditions, *Adv. Mater. Process. Technol.*, 2023, **9**(4), p 1524-1540.

9. Y. Dilay, Determination of Wear Resistance of Nickel-Carbide Alloy Coating by Atmospheric Plasma Spray Technique on 30MnB5 Alloy Steel Used in Cultivator Blades, *Mater. Res. Express.*, 2023, **10**(6), p 066504.

10. Jia, H., Zhao, J., Zhao, X., Yin, B., Liu, J., Hao, J., & Zhao, X. Discrete Element Parameter Calibration and Wear Characteristics Analysis of Soil-Rotary Tillage Blade in Gneiss Mountainous Area. (2023)

11. S. Ma, L. Xu, S. Xu, H. Tan, J. Song and C. Shen, Wear Study on Flexible Brush-Type Soil Removal Component for Removing Soil Used to Protect Grapevines Against Cold, *Biosys. Eng.*, 2023, **228**, p 88-104.

12. X. Zhang, L. Zhang, X. Hu, H. Wang and X. Shi, Calibrating Contact Parameters of Typical Rotary Tillage Components Cutting Soil Based on Different Simulation Methods, *Sci. Rep.*, 2023, **13**(1), p 5757.

13. L.C. Vlădutoiu, G. Chişiu, A. Tudor, N.V. Vlădut, L. Fechete Tutunaru, E. Marin and I.A. Grigore, Tribological Study of Chisel Knives in Sandy Soil, *Agriculture*, 2023, **13**(6), p 1235.

14. Szala, M., Szafran, M., Matijošius, J., & Drozd, K. Abrasive Wear Mechanisms of S235JR, S355J2, C45, AISI 304, and Hardox 500 Steels Tested Using Garnet, Corundum and Carborundum Abrasives. Adv. Sci. Technol. Res. J. 17(2) (2023)

15. Y. Wang, C. Lu, J. Chen, C. Cui, Y. Pan, W. Pfleging and J. Sun, Effects of self-Healing Biomimetic Subsoiler on Tillage Resistance, Wear-Corrosion Performance and Soil Disturbance Morphology Under Different Soil Types, *Int. J. Agric. Biol. Eng.*, 2023, **16**(3), p 7-14.

16. J. Selech, W. Majchrzycki and D. Ulbrich, Field and Laboratory Wear Tests of Machine Components Used for Renovation of Dirt Roads—A Case Study, *Materials*, 2023, **16**(18), p 6180.

17. Y.S. Saygili and B. Cakmak, Improvement of Wear Resistance in Toothed Harrows Coated with HVOF and PVD Methods, *J. Agric. Sci. Technol.*, 2023, **25**(1), p 47-59.

18. Umashankar, D., Thakshak, D. S., Nayaka, D. J., Hiremath, S. R., & Suhas, R. D. Molybdenum Powder Coating on Steel Substrate to Study Three Body Wear Resistance. In IOP Conference Series: Materials Science and Engineering (Vol. 1291, No. 1, p. 012012). IOP Publishing (2023).

19. V. Singh, A.K. Singla and A. Bansal, Wetting and Erosive Behavior of VC-TiC+ CuNi-Cr Based Coatings Developed by HVOF: Role of Laser Texturing, *Eng. Fail. Anal.*, 2023, **152**, 107479.

20. G. Bolelli, C. Lyphout, L.M. Berger, V. Testa, H. Myalska-Głowacka, P. Puddu, P. Sassatelli and L. Lusvarghi, Wear Resistance of HVOF-and HVAF-Sprayed (Ti, Mo)(C, N)-Ni Coatings from an Agglomerated and Sintered Powder, *Wear*, 2023, **15**(512), p 204550.

21. F.L. Toma, A. Meyer, O. Kunze, I. Shakhverdova, B. Matthey, F. Härtwig and S. Makowski, Microstructural Characterization and Oscillating Sliding Wear Investigations of the Aqueous Suspension Sprayed HVOF WC-12Co Coatings, *J. Therm. Spray Technol.*, 2023, **32**(23), p 456-472.

22. S. Hong, D. Mei, J. Wu, J. Lin, Y. Wu, J. Li and Y. Zheng, Hydro-Abrasive Erosion and Cavitation-Silt Erosion Characteristics of HVOF sprayed WC-Ni Cermet Coatings under Different Flow Velocities and Sand Concentrations, *Ceram. Int.*, 2023, **49**(1), p 74-83.

23. S. Hong, Z. Wang, J. Lin, J. Cheng, W. Sun and Y. Zheng, Hydro-Abrasive Erosion Behaviors of HVOF Sprayed Carbide-Based Cermet Coatings in Simulated Seawater Slurries, *Tribol. Int.*, 2023, **177**, 108001.

24. D. Ozkan, Structural Characteristics and Wear, Oxidation, Hot Corrosion Behaviors of HVOF Sprayed $Cr_3C_2$-NiCr Hardmetal Coatings, *Surf. Coat. Technol.*, 2023, **457**, 129319.

25. Z.A. Abbasi, A. Mateen, M. Abbas, M.A.U. Rehman and A. Wadood, Improved Tribological and Electrochemical Behavior of Concentrated Chromite Coatings Developed by HVOF and Plasma Spray Techniques, *J. Market. Res.*, 2023, **26**, p 9079-9094.

26. R. Suraj, Hardfacing and its Effect on Wear and Corrossion Performance of Various Ferrous Welded Mild Steels, *Mater. Today Proceed.*, 2021, **42**, p 842-850.

27. G.S. Rethnam, S. Manivel, V.K. Sharma, C. Srinivas, A. Afzal, R.K.A. Razak and C.A. Saleel, Parameter Study on Friction Surfacing of AISI316Ti Stainless Steel over EN8 Carbon Steel and its Effect on Coating Dimensions and Bond Strength, *Materials*, 2021, **14**(17), p 4967.

28. E. Katinas, M. Antonov, V. Jankauskas and D. Goljandin, Effect of Local Remelting and Recycled WC-Co Composite

Reinforcement Size on Abrasive and Erosive Wear of Manual Arc Welded Hardfacings, *Coatings*, 2023, **13**(4), p 734.

29. Ribu, D. C., Rajesh, R., Thirumalaikumarasamy, D., Vignesh, S., & Paventhan, R. Development of Empirical Relationships to Predict Porosity and Hardness of WC-10Co Coatings on 35CrMo Steel Using DOE Approach. In *AIP Conference Proceedings* (Vol. 2395, No. 1). AIP Publishing (2021).

30. D.K. Goyal, H. Singh and H. Kumar, An Overview of Slurry Erosion Control by the Application of High Velocity Oxy Fuel Sprayed Coatings, *Proceed. Inst. Mech. Eng. Part J J. Eng. Tribol.*, 2011, **225**(11), p 1092-1105.

31. H. Raushan, A. Bansal, V. Singh, A.K. Singla, J. Singla, A. Omer, J. Singh, D.K. Goyal, N. Khanna and R.S. Rooprai, Dry Sliding and Slurry Abrasion Behaviour of Wire Arc Additive Manufacturing-Cold Metal Transfer (WAAM-CMT) Cladded Inconel 625 on EN8 Steel, *Tribol. Int.*, 2023, **1**(179), p 108176.

32. Bhardwaj, B. P. *Steel and Iron Handbook*. NIIR project consultancy services (2014).

33. D. Kumar and P. Mohanraj, Design and Analysis of Rotavator Blades for its Enhanced Performance in Tractors, *Asian J. Appl. Sci. Technol. AJAST*, 2017, **1**(1), p 160-185.

34. H. Singh, M. Kumar and R. Singh, Microstructural and Mechanical Characterization of a Cold-Sprayed WC-12Co Composite Coating on Stainless Steel Hydroturbine Blades, *J. Therm. Spray Technol.*, 2023, **32**(4), p 970-983.

35. L. Zhicheng, S. Jiangzheng, H. Chuang, W. Fan and K. Dejun, Effect of Laser Power on Microstructure and Tribological Performance of WC− 10Co4Cr Coating, *Int. J. Appl. Ceram. Technol.*, 2023, **20**(5), p 2847-2859.

36. V. Singh, A.K. Singla and A. Bansal, Influence of TiC Content on Slurry Erosion Behaviour of HVOF Sprayed Titanium Carbide and Cupronickel-Chromium Based Coatings, *J. Therm. Spray Technol.*, 2023, **32**(6), p 1739-1757.

37. V. Singh, A.K. Singla and A. Bansal, Influence of Laser Texturing Along with PTFE Topcoat on Slurry and Cavitation Erosion Resistance of HVOF Sprayed VC Coating, *Surf. Coat. Technol.*, 2023, **470**, 129858.

38. R.S. Rooprai, A. Bansal and J. Singh, Influence of TiC Powder Content on wear Behaviour of Inconel 625 Clads Developed by Hybrid-Mode Wire Arc Additive Manufacturing (WAAM) on EN-8 Steel, *Tribol. Int.*, 2023, **189**, 108937.

39. H.I. Kurt, U.B. Akyüz and E. Ergül, Mechanical Changes and Analysis of Heat-Treated 4140 Steel with Taguchi Method and ANOVA, *Int. J. Mater. Eng. Technol.*, 2023, **6**(1), p 1-6.

40. R. Khuengpukheiw, A. Wisitsoraat and C. Saikaew, Wear Behaviors of HVOF-Sprayed NiSiCrFeB, WC-Co/NiSiCrFeB and WC-Co Coatings Evaluated Using a Pin-on-Disc Tester with C45 Steel Pins, *Wear*, 2021, **484**, 203699.

41. A. Natsis, G. Papadakis and J. Pitsilis, The Influence of Soil Type, Soil Water and Share Sharpness of a Mouldboard Plough on Energy Consumption, Rate of Work and Tillage Quality, *J. Agric. Eng. Res.*, 1999, **72**(2), p 171-176.